Biophysical Journal
Article

Biophysical Society

NMR Analysis of Amide Hydrogen Exchange Rates in a Pentapeptide-Repeat Protein from *A. thaliana*

Shenyuan Xu,[1] Shuisong Ni,[1] and Michael A. Kennedy[1,*]
[1]Department of Chemistry and Biochemistry, Miami University, Oxford, Ohio

ABSTRACT At2g44920 from *Arabidopsis thaliana* is a pentapeptide-repeat protein (PRP) composed of 25 repeats capped by N- and C-terminal α-helices. PRP structures are dominated by four-sided right-handed β-helices typically consisting of mixtures of type II and type IV β-turns. PRPs adopt repeated five-residue (Rfr) folds with an Rfr consensus sequence (STAV)(D/N)(L/F)(S/T/R)(X). Unlike other PRPs, At2g44920 consists exclusively of type II β-turns. At2g44920 is predicted to be located in the thylakoid lumen although its biochemical function remains unknown. Given its unusual structure, we investigated the biophysical properties of At2g44920 as a representative of the β-helix family to determine if it had exceptional global stability, backbone dynamics, or amide hydrogen exchange rates. Circular dichroism measurements yielded a melting point of 62.8°C, indicating unexceptional global thermal stability. Nuclear spin relaxation measurements indicated that the Rfr-fold core was rigid with order parameters ranging from 0.7 to 0.9. At2g44920 exhibited a striking range of amide hydrogen exchange rates spanning 10 orders of magnitude, with lifetimes ranging from minutes to several months. A weak correlation was found among hydrogen exchange rates, hydrogen bonding energies, and amino acid solvent-accessible areas. Analysis of contributions from fast (approximately picosecond to nanosecond) backbone dynamics to amide hydrogen exchange rates revealed that the average order parameter of amides undergoing fast exchange was significantly smaller compared to those undergoing slow exchange. Importantly, the activation energies for amide hydrogen exchange were found to be generally higher for the slowest exchanging amides in the central Rfr coil and decreased toward the terminal coils. This could be explained by assuming that the concerted motions of two preceding or following coils required for hydrogen bond disruption and amide hydrogen exchange have a higher activation energy compared to that required for displacement of a single coil to facilitate amide hydrogen exchange in either the terminal or penultimate coils.

INTRODUCTION

At2g44920 from *Arabidopsis thaliana* is a member of the distinctive family of pentapeptide-repeat proteins (PRPs) that contain at least eight tandem repeats consisting of the approximate consensus sequence (STAV)(D/N)(L/F)(S/T/R)(X), as discovered by Bateman et al. (1). Four consecutive pentapeptide repeats form a square coil, and the coils stack to form a right-handed quadrilateral β-helix. As a consequence, PRPs adopt a repeated five-residue (Rfr) fold with stacked pentapeptide repeats defining the faces of the Rfr-fold (2,3). Each coil completes a revolution with 20 amino acids and travels ~4.8 Å along the β-helix axis. The distance between $C_\alpha(i)$ to $C_\alpha(i+3)$ is <7.0 Å in tandem pentapeptide repeats, which is a common feature of four-residue β-turns if the residues are not in an α-helix (4,5). Pentapeptide repeats contain a β-bridge ($i-1$ residue in each consensus sequence), which is a feature of β-turns that effects a change in direction of the protein backbone (4,5). The universal four-residue turns that shape PRPs are classified into type II and type IV β-turns based on the main chain (Φ, Ψ) dihedral values of the central two residues, $i+1$ and $i+2$ (6). The Ψ-torsion angle of i and the Φ-torsion angle of $i+1$ differ between type II and type IV turns by an ~90° rotation of the peptide unit between these two residues, resulting in different networks of intercoil and intracoil hydrogen bonding patterns (7). Structural analyses of two PRPs, Rfr32, and MfpA, revealed that the Rfr-fold is shaped by pentapeptide repeats adopting type II and type IV β-turns, indicating that these two turns may be universal motifs in all 2110 PRPs identified in the Pfam database that form the Rfr-fold (7). Whereas PRP structures are unusual in that they form right-handed β-helices composed purely of type II β-turns and type IV β-turns plus associated stacked β-bridges or β-ladders, At2g44920 appears rare even among PRPs, in that it is the only PRP structure known to date whose turns are made up exclusively of type II β-turns.

Submitted September 22, 2016, and accepted for publication April 10, 2017.
*Correspondence: kennedm4@miamioh.edu
Editor: Jeff Peng.
http://dx.doi.org/10.1016/j.bpj.2017.04.016

Given the unique structure of At2g44920, we decided to investigate its biophysical properties to determine if it had unusual structural stability. In addition to structural stability, we were also quite interested to determine if At2g44920 exhibited any unusual amide hydrogen exchange rates. Because the hydrogen-bonding network of the Rfr-fold core of At2g44920 is well defined from its crystal structure (8), and given its unique structure, At2g44920 serves as an excellent model to investigate structural and dynamic factors that govern amide hydrogen exchange rates. Knowledge of protein dynamics is essential to understanding transient protein structure that fluctuates on different timescales, which are essential for amide exchange events to occur in folded proteins. Nuclear magnetic resonance (NMR) is a powerful technique to study protein dynamics over a wide range of timescales with single amino-acid-specific resolution and without modification to the protein structure (9–12). Amide hydrogen exchange rates measured by NMR can be used to characterize the dynamics of backbone amide groups with lifetimes on the 0.01–1 s timescale using the Phase-Modulated CLEAN Chemical Exchange (CLEANEX-PM) experiment for fast exchange measurements (13) and the two-dimensional (2D) HSQC NMR experiment for slow exchange measurements for amide exchange lifetimes in the range 10^3–10^7 s (14). In the native-state hydrogen deuterium exchange (HDX) NMR experiment, the exchange rate of an amide proton is measured by monitoring the exponential decay of the proton signal intensity when the folded protein is exposed to deuterated solvent. Using nuclear spin relaxation measurements, protein backbone dynamic motions on the picosecond to nanosecond timescale can be probed by monitoring longitudinal R_1 relaxation rates, transverse R_2 relaxation rates, and heteronuclear nuclear Overhauser effects (hnNOEs) for each amino acid (15–17). The R_1, R_2, and hnNOEs can be used to calculate spectral density functions $J(\omega)$ that quantify the amount of motion present capable of producing oscillating magnetic fields at MHz frequencies (9,12) that drive spin relaxation due to fluctuating magnetic fields caused by time-dependent dipole-dipole interactions, chemical shift anisotropy, and quadrupolar interactions. Model free analysis is used to extract the approximately nanosecond molecular rotation and approximately picosecond internal motion from R_1, R_2, hnNOE data, and the site-specific squared order parameter S^2 is widely reported (10,18). The order parameter S^2 indicates the degree to which the internal motion of bond vector is restricted within a cone of angle θ, with larger values of S^2 corresponding to smaller θ (19). The values of S^2 range from 0 to 1, with 0 representing unrestricted reorientation of the bond vector and 1 indicating a completely rigid bond vector on the timescale for which the relaxation measurements are sensitive (20).

Amide hydrogen exchange rates in proteins are widely interpreted using the Linderstrøm-Lang equation (21). The modified modern equation demonstrating the two-step exchange mechanism was given by Hvidt (22) in 1964, as follows:

$$\mathrm{NH(cl)} \underset{k2}{\overset{k1}{\rightleftarrows}} \mathrm{NH(op)} \xrightarrow{k3} \text{exchanged.}$$

In this reaction scheme, *NH*(*cl*) and *NH*(*op*) represent exchange-resistant and exchange-competent forms of the proteins, respectively. According to this model, the apparent equilibrium constant is the ratio between the opening rate constant and the closing rate constant, $K_{\mathrm{op}} = (k_{\mathrm{op}}/k_{\mathrm{cl}})$. Exchange can occur once the protein experiences motions that bring the amide hydrogen to an exchange-accessible state. Such motions include local motions that break single hydrogen bonds, conformational fluctuations of segments of the protein chain, and local or global unfolding (23). The observed exchange rate constant can be expressed by the following:

$$k_{\mathrm{ex}} = k_1 k_3 / k_1 + k_2 + k_3.$$

There are two limiting mechanisms to describe the HX kinetics depending on the relative rate between k_2 and k_3: EX2 indicates $k_3 << k_2$ and EX1 indicates $k_3 >> k_2$. The two mechanisms are found in the pH range above pH 3 and can be interconverted depending on the experimental conditions. For example, a transition from EX2 to EX1 exchange was observed by Hvidt and Nielsen (24) while increasing pH. They found that in the EX2 regime, the exchange rates increased linearly with pH whereas exchange was almost pH-independent in the EX1 regime. Alternatively, the EX1 limit is often correlated with global unfolding (25) whereas interpretation of the EX2 limit can be correlated with global unfolding, local fluctuations, and subglobal motions by varying experimental conditions (26). Partially folded intermediates, referred to as "foldons", have been observed in cytochrome *c* based on the sensitivity of exchange rates of different residues on denaturant (27). However, no nativelike partially folded, exchange-accessible, foldon was been detected for chymotrypsin inhibitor 2 as their exchange rates merge together at high GdmCl concentrations indicating the global unfolding reaction (28). Whether the exchange of amide hydrogen occurs locally or globally can be classified experimentally by observing its denaturant dependence (29), temperature dependence (30), or mutagenesis (31).

In this study, the global stability of At2g44920 was characterized using NMR and circular dichroism (CD) spectroscopy. Protein backbone dynamics characterized by S^2 values were determined from R_1, R_2, and hnNOE measurements and found to vary with a specific pattern within the PRP sequence. Finally, the amide hydrogen exchange rates were measured and found to span ~10 orders of magnitude even though essentially all the amide groups occur on the surface of the protein. Our analysis indicates that, on

average, amino acids with the largest protection factors formed stronger hydrogen bonds, were exposed to smaller solvent-accessible surface areas, had more restricted fast motion, and were associated with higher activation energies for amide hydrogen bond exchange.

MATERIALS AND METHODS

Protein expression and purification

Preparation of the expression vector pET28b (Novagen, Madison, WI) for At2g44920 with 6×histidine tags at both the N- and C termini was as described in Ni et al. (8). The plasmid construct was transformed into the host strain *Escherichia coli* BL21 (DE3) for expressing the protein. The culture was grown in ^{15}N-labeled and ^{13}C-labeled M9 medium with vigorous shaking at 310 K supplemented with 30 μg mL^{-1} kanamycin until the optical density at 600 nm reached ~0.8. Protein expression was induced at 301 K overnight. The cell pellet was harvested after centrifuging 20 min at 5000 × *g* and resuspended in the 30 mL lysis buffer (20 mM Tris pH 7.8, 250 mM NaCl, 10% glycerol). Cell lysis was achieved by passing suspended cells through a French press (Thermo Fisher Scientific, Waltham, MA) four times, then the cell lysate was centrifuged at 12,000 × *g* for 30 min. The supernatant was loaded onto a Nickel-NTA Superflow column (Qiagen, Hilden, Germany) preequilibrated with 50 mL buffer (20 mM Tris pH 7.8, 250 mM NaCl, 10% glycerol), and was washed stepwise with the same buffer containing 0 and 30 mM imidazole. At2g44920 was eluted from Ni-NTA affinity column with buffer (20 mM Tris pH 7.8, 250 mM NaCl, 10% glycerol) containing 300 mM imidazole. The purified At2g44920 was put into a dialysis bag with a molecular mass cutoff of 12,000–14,000 Da (Thermo Fisher Scientific) and the protein was concentrated by placing the dialysis bag containing the protein solution into a plastic weighing tray containing powdered polyethylene glycol 20,000 (Alfa Aesar, Ward Hill, MA), resulting in water absorption across the dialysis membrane. The final sample concentration was adjusted to ~1 mM using the same buffer with 10% (v/v) D_2O for NMR experiments.

NMR spectroscopy and backbone resonance assignments

The double-labeled ^{15}N, ^{13}C-At2g44920 sample was put into 5-mm Shigemi NMR tubes and spectra were collected at 308 K on a 600 MHz Inova spectrometer (Varian, Palo Alto, CA) with a 5-mm HCN room temperature probe. Backbone assignments were made based on the following three-dimensional spectra: HNCACB, CBCA(CO)NH, HNCO, HN(CA)CO, HNCA, and (H)CC(CO)NH-TOCSY. Spectra were processed with the software NMRPipe (32) and visualized with the software SPARKY 3.114 (33). The backbone ^{1}H, ^{13}C, and ^{15}N resonance assignments were first made using the PINE server (34), then manually confirmed through SPARKY 3.114.

CD spectroscopy and thermal protein denaturation

CD experiments were performed with a model No. 215 CD spectrophotometer (Aviv Biomedical, Lakewood, NJ) using 0.5-mm quartz cuvettes. Proteins were dialyzed into buffer (20 mM potassium phosphate pH 7.8, 150 mM NaF) suitable for CD spectroscopy and the protein concentration was adjusted to 1 mg mL^{-1}. To determine the secondary structure of At2g44920, a far-UV wavelength spectrum between 170 and 300 nm was recorded. A thermal denaturation curve for At2g44920 was obtained by recording the ellipticity at 218 nm from 20 to 80°C with 1°C interval. The spectrum was recorded by averaging three consecutive scans with a bandwidth of 1.0 nm and a time constant of 1.0 s. The wavelength spectrum was processed by first subtracting a blank spectrum followed by baseline correction and noise reduction.

NMR measurements of thermal protein denaturation

To identify individual amino acids that might indicate early local unfolding of At2g44920, a series of 2D ^{1}H-^{15}N HSQC spectra were recorded in the 300–338 K range. The protein was heated with temperature increments of ~5.0 K until denatured. Temperature calibration for each spectrometer was performed using 100% ethylene glycol ($OHCH_2CH_2OH$) following standard procedures.

Hydrogen exchange experiments

Hydrogen exchange data were collected using a room temperature probe on an 850-MHz Avance III NMR spectrometer (Bruker, Billerica, MA) at 308 K, the same temperature at which the chemical shifts were assigned. Hydrogen-deuterium exchange experiments were initiated by exchanging the lyophilized protein (20 mM Tris pH 7.8, 250 mM NaCl) into 100% D_2O. Then a series of ^{1}H-^{15}N HSQC spectra were immediately collected to monitor the decay of the ^{1}H signal as the ^{1}H is replaced by ^{2}H due to exchange. The exchange rates were quantified by fitting the cross-peak volumes as a function of time to a single exponential decay. Relatively fast ^{1}H exchange rates were measured with CLEANEX-PM pulse sequence described by Hwang et al. (13,35). The following mixing times for the CLEANEX-PM spin-locking were used: 5, 6, 8, 10, 12, 15, 18, and 20 ms. The spin-locking γB_1 field in CLEANEX-PM was 8.3 kHz. The number of complex spectral points were 2048 and 96 in the t_2 and t_1 dimensions, respectively; the spectral widths were 15,243.902 and 3015.252 Hz in t_2 and t_1 dimensions, respectively; and the acquisition times were 67.2 and 31.8 ms in the t_2 and t_1 dimensions, respectively. The number of transients was set to 128 and the recycle delay for each scan was 2 s. The cross-peak intensity V_0 in the following fitting equation was obtained from a reference ^{1}H-^{15}N fast HSQC spectrum:

$$\frac{V}{V_0} = \frac{k}{\left(R_{1A,app} + k - R_{1B,app}\right)} \times \left\{\exp\left(-R_{1B,app}\tau_m\right) - \exp\left[-\left(R_{1A,app} + k\right)\tau_m\right]\right\}, \quad (1)$$

where k is the normalized exchange rate; $R_{1A,app}$ is a combination of longitudinal and transverse relaxation rates, which depends on the trajectory of magnetization; $R_{1B,app}$ is the apparent solvent relaxation rate, which was determined to be 0.6 Hz for the CLEANEX-PM; and V is the peak volume obtained from each ^{1}H-^{15}N FHSQC corresponding to each mixing time τ_m. The exchange rate k and hydrogen relaxation rate $R_{1A,app}$ were determined by fitting the intensity buildups as a function of mixing times. The exchange rates k_{ex} for amide protons were corrected by dividing k by 0.85 due to the water saturation effect in the CLEANEX-PM experiment.

The hydrogen-deuterium exchange experiments were repeated at 298 and 313 K. After obtaining exchange rates at different temperatures, the Arrhenius equation was used to fit the temperature dependence of exchange rates. The energies of activation for hydrogen deuterium exchange were determined from fitting the temperature-dependent hydrogen exchange data using the Arrhenius equation.

Backbone ^{15}N relaxation experiments

All 2D ^{1}H-^{15}N HSQC spectra for the ^{15}N relaxation measurements were collected at two different magnetic fields with a 600-MHz Avance III spectrometer and an 850-MHz Avance III NMR spectrometer (both by Bruker). The temperature used was 308 K. The nitrogen-15 T_1 values were measured

using hsqct1etf3gpsi3d, and delay times were set at 100, 200, 300, 400, 600, 800, 1000, 1500, 1700, and 2200 ms. The nitrogen-15 T_2 values were measured using hsqct2etf3gpsi3d, and the loop counters for the CPMG pulse train were set at 1, 2, 3, 4, 5, 7, 10, 12, 15, and 20. The length of a single CPMG loop was 16.96 ms in the experiment setup, with the T_2 delay times corresponding to 16.96, 33.92, 50.88, 67.84, 84.80, 118.72, 169.60, 203.52, 254.40, and 339.20 ms. The ^{1}H-^{15}N heteronuclear NOE were measured by employing the pulse sequence hsqcnoef3gpsi, and the steady-state ^{15}N{^{1}H} NOE values were obtained by the ratio of peak intensities with and without a 3 s proton saturation. The recycle delay was set to 10 s to allow the ^{15}N and ^{1}H spins to return to equilibrium. All data were collected in an interleaved manner and triplicate data sets were recorded to determine the error bars for each parameter.

The R_1 and R_2 relaxation rates and the ^{1}H-^{15}N heteronuclear NOE were fitted using the program Relax (36). Peak intensity errors were calculated from triplicate data sets and 500 step Monte Carlo simulations were used to determine parameter errors. The model-free analysis was carried with the Relax software using the, to our knowledge, new model-free optimization "d'Auvergne protocol" (37,38). Nine model-free models were used in this protocol: m0 = {}, m1 = {S^2}, m2 = {S^2, τ_e}, m3 = {S^2, R_{ex}}, m4 = {S^2, τ_e, R_{ex}}, m5 = {S^2, S^2_f, τ_s}, m6 = {S^2, τ_f, S^2_f, τ_s}, m7 = {S^2, S^2_f, τ_s, R_{ex}}, m8 = {S^2, $\tau_f S^2_f$, τ_s, R_{ex}}, and m9 = {R_{ex}}. The model m0 assumes no internal motions are statistically significant. Five diffusion tensors were implemented within Relax, the ellipsoid, the prolate spheroid, the oblate spheroid, the sphere, and the local τ_m model. In general, the model-free models were optimized and selected in the absence of any global diffusion parameters by incorporating a local correlation time parameter, τ_m, into the local t_m tensor. The assumption of constructing this local t_m tensor was that the overall rotational diffusion of each bond could be estimated by its individual correlation time (τ_m) as each spin system tumbles independently. The local t_m model was used to optimize the diffusion parameters from the spherical, prolate spheroid, oblate spheroid, and ellipsoid tensors. The universal solution that best described the dynamics of all spin systems was determined after iterative steps of optimizing models m0–m9 with the diffusion parameters fixed, model elimination, and AIC model selection until convergence.

RESULTS

Structure of At2g44920

The structure of At2g44920 (residues 81–224) has a characteristic Rfr-fold core composed of five uninterrupted coils made up of 25 pentapeptide repeats and α-helical elements capping both termini (Fig. 1). Every four consecutive pentapeptide repeats form a right-handed quadrilateral β-helical coil with each pentapeptide repeat occupying one face of the coil. The center residue of each pentapeptide repeat is designated with symbol i, its following residues are designated i+1 and i+2, and its preceding residues designated i−1 and i−2. The side chains of residues i and i−2 of each pentapeptide repeat point toward the interior of the Rfr-fold core (Fig. 2 *A*). The i−2 position is dominated by the small hydrophobic residue Ala, and the i residue is mostly occupied by large hydrophobic residues Leu and Phe, and sometimes Val, Ile, or Met. The alternation between large and small hydrophobic side chains of the i and i−2 residues make the interior of At2g22920 highly hydrophobic and devoid of water. Stacking of hydrophobic residues in each coil is undoubtedly important in stabilizing the Rfr-fold. The side chains of the remaining amino acids (i−1, i+1, and i+2) in each pentapeptide repeat point away from the Rfr-fold core (Fig. 2 *B*) and these residues determine the surface-charge distribution of At2g44920. Like other PRPs, At2g44920 has α-helical elements capping both N- and C termini. The two α-helices at the C terminus are linked by a disulfide bridge with a conserved loop between helices. Unlike other PRPs, which are shaped by mixtures of type II and type IV β-turns, At2g44920 is composed only of type II β-turns based on the main chain (Φ, Ψ) analysis (Fig. 2 *C*). As a consequence, this makes the structure and hydrogen-bonding pattern of At2g44920 unique (Fig. 2 *D*). In the Rfr-fold structure, the carbonyl oxygen of i residue forms an intracoil hydrogen bond with the amide proton of i−2 residue of the following pentapeptide repeat, thus constituting a type II β-turn. The amide and carbonyl groups of the rest of the amino acids in the pentapeptide repeat can form intercoil hydrogen bonds with the main chain atoms of the pentapeptide repeat above and below because the i−1 β-bridge residue contributes both an amide proton and carbonyl oxygen to the intercoil hydrogen bonding.

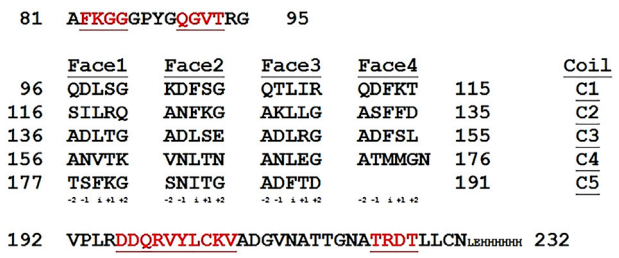

FIGURE 1 Shown here is the sequence overview of At2g44920. The N-terminus is defined by residues 81–95 and the C terminus is defined by residues 192–232. Residues 96–191 are organized into stacked PRPs for each face of coils C1–C5. The i−2 to i+2 positions of the PRPs are indicated at the bottom of the stack of PRPs. The underlined/red letters indicate α-helical residues in both termini. To see this figure in color, go online.

CD study of global stability

CD spectroscopy is a powerful tool that enables evaluation of the secondary structure and folding properties of proteins (39). The CD spectra of α-helices and β-sheets are well characterized. Alpha-helical proteins have negative bands at 222 and 208 nm and a positive band at 193 nm (40), whereas antiparallel β-sheets possess a negative band at 218 nm and a positive band at 195 nm (41). The CD spectra of different types of β-turns, however, remain ambiguous (42), in part due to the lack of model proteins that contain exclusively one type of β-turn. Interestingly, the crystal structure of At2g44920 shows that the Rfr-fold (95 residues) is a right-handed quadrilateral β-helix composed purely of type II β-turns plus β-bridges. Consequently, its CD spectrum should be dominated by type II β-turns and stacked β-bridges. The far-UV CD spectrum of At2g44920 was dominated by a minimum band at

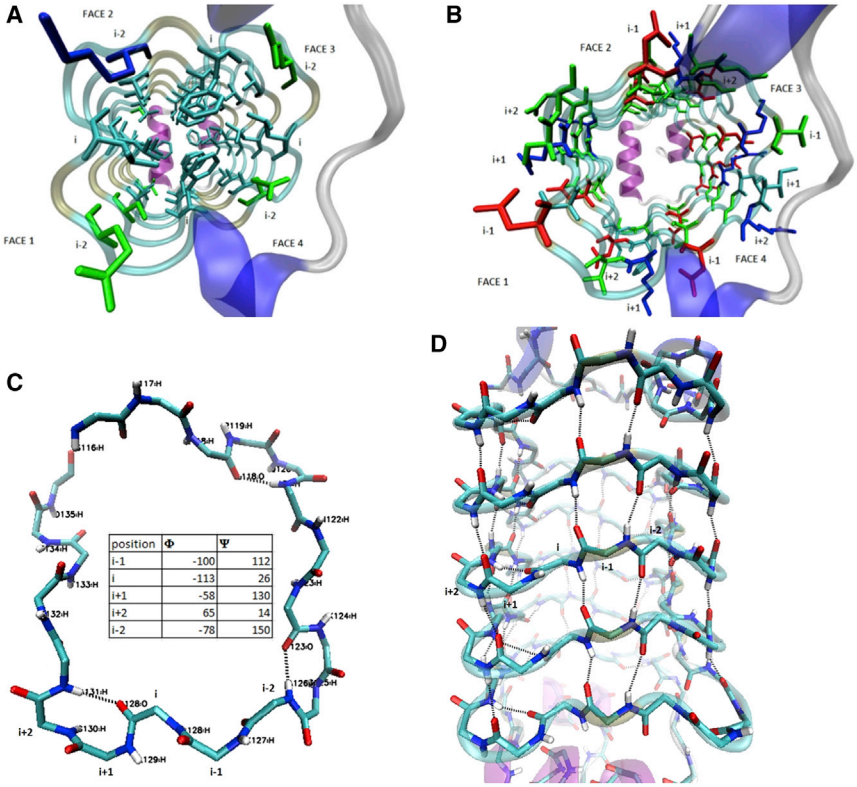

FIGURE 2 Shown here is the four-sided right-handed β-helices of the At2g44920 Rfr-fold. Each pentapeptide repeat has five amino acids. The center residue is designated with symbol i with the following residues labeled $i+1$ and $i+2$ and the preceding residues labeled $i-1$ and $i-2$. (*A*) The side chains of residue i and residue $i-2$ of each pentapeptide repeat point toward the interior of the Rfr-fold core, forming the hydrophobic core. (*B*) The side chains of the remaining amino acids $i-1$, $i+1$, and $i+2$ within each pentapeptide repeat all point away from the Rfr-fold core. (*C*) The average main chain (Φ, Ψ) dihedral torsion angle pair for each residue in the pentapeptide repeat was put inside the coil. The main chain (Φ, Ψ) dihedral torsion angle for residue $i+1$ and $i+2$ in a typical type II β-turn are ($-55/130$) and (65/10), respectively. In the type-II β-turn, the carbonyl groups of residues i and $i+2$ and the amide groups of residues $i+1$ and $i-2$ of the following pentapeptide repeat are almost orthogonal to the plane of the β-sheets. Consequently, an intracoil hydrogen bond is formed between the carbonyl group of i and amide proton of $i-2$ of the following pentapeptide unit. (*D*) The amide and carbonyl group of the remaining residues in the pentapeptide repeat form intercoil hydrogen bonds with residues in another pentapeptide repeat above and below it. To see this figure in color, go online.

$\sim$214 nm (Fig. S1 *a*). Even with α-helices at both N- and C-termini, the characteristic CD features of α-helices were buried under those characteristic of type II β-turns and parallel β-bridges, which dominate the At2g44920 structure. CD melting experiments were carried out to determine the global melting temperature of At2g44920. The ellipticity at 218 nm was measured as a function of temperature from 20 to 80°C in 1°C increments. The T_m was $\sim$62.8°C (Fig. S1 *b*) and the enthalpy of folding was ~-120 kcal/mol, indicating that At2g44920 is thermally stable. The percent folded protein as a function of temperature is shown in Fig. S1 *c*. The T_m of 62.8°C for At2g44920 is almost exactly equal to the average T_m of 62.2°C for >1100 proteins (Fig. S1 *d*) for which thermodynamic parameters are compiled in the ProTherm database (43), indicating that the global stability of At2g44920 is not unusual.

Temperature-dependent NMR study of stability of local structural melting

Although the CD thermal melting experiment provides information about cooperative global unfolding of At2g44920, a series of 2D ^{1}H-^{15}N HSQC spectra were recorded between 300 and 338 K to provide insight into thermal unfolding pathway at the individual amino acid level. The 2D ^{1}H-^{15}N HSQC spectra of At2g44920 is of excellent quality (Fig. 3). Residues whose proton and nitrogen resonances shifted or disappeared with increasing temperature relative to 308 K (Fig. S2) were plotted on the structure of At2g44920 in Fig. 4. More than half of the cross peaks disappeared or the peak intensities decreased dramatically at $\sim$335 K (62°C), a temperature almost identical to the global T_m (62.8°C) determined by the CD melting experiment. The protein completely denatured at $\sim$338 K as peaks collapsed

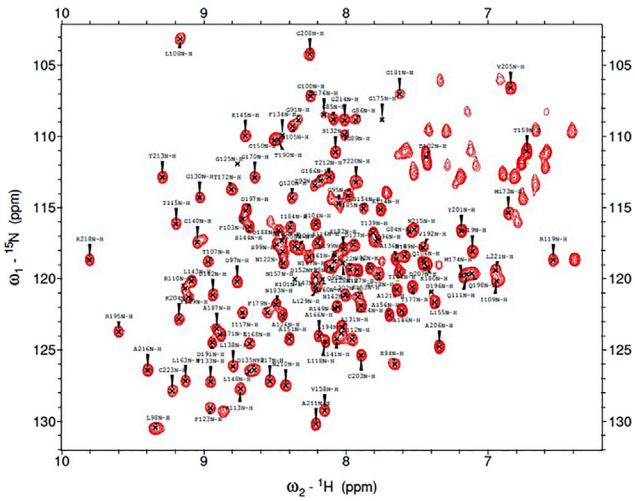

FIGURE 3 Shown here is the ^{1}H-^{15}N HSQC spectrum of At2g44920 collected at 850 MHz and 308 K. Individual resonance assignments are indicated by labels. To see this figure in color, go online.

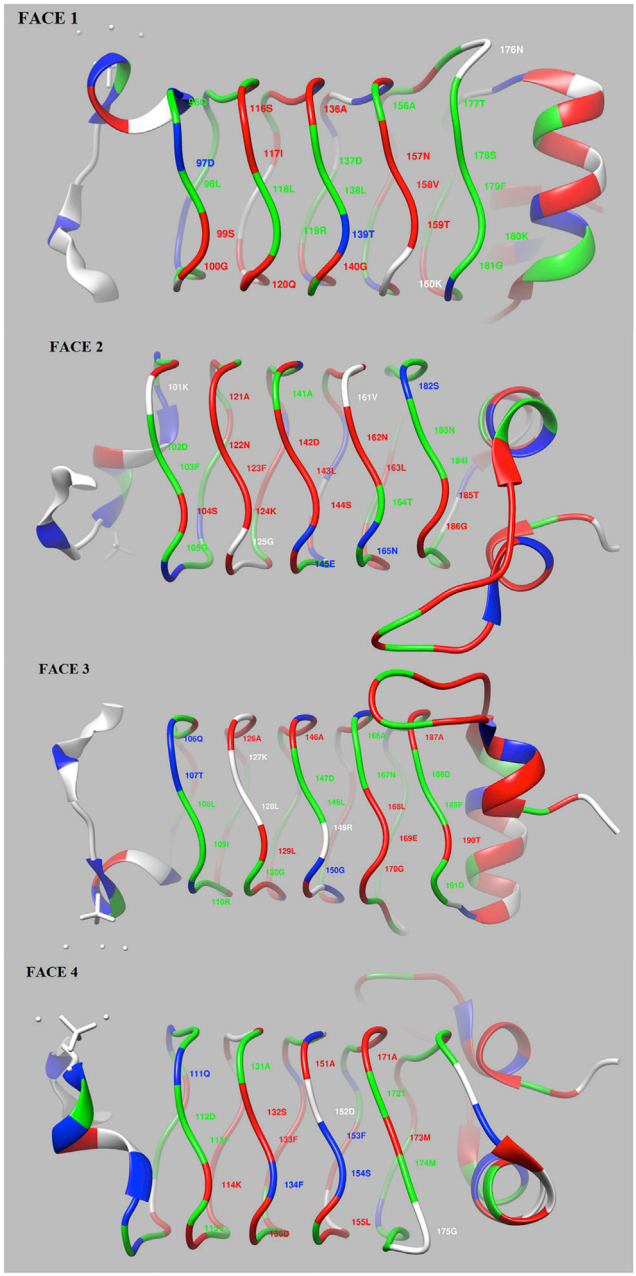

FIGURE 4 Shown here is the mapping of temperature-labile amino acids onto the structure of At2g44920 based on temperature-dependent NMR measurements. For peaks present at 334 K: red (*dark gray*), $^{1}H < 0.11$ ppm and $^{15}N < 0.4$ ppm; green (*light gray*), $^{1}H = 0.11$–0.15 ppm and $^{15}N = 0.4$–1 ppm; and blue (*black*), $^{1}H = > 0.15$ ppm and $^{15}N > 1$ ppm. For peaks present between 327 and 334 K: red (*dark gray*), $^{1}H < 0.05$ ppm and $^{15}N < 0.2$ ppm; green (*light gray*), ^{1}H 0.05–0.11 ppm or ^{15}N 0.2–0.5 ppm; and blue (*black*), $^{1}H > 0.11$ ppm or $^{15}N > 0.5$ ppm. To see this figure in color, go online.

to the center of the proton spectrum chemical shift range. Peaks that disappeared or shifted between 300 and 335 K indicated amino acids at sites where thermal destabilization of the secondary or tertiary structure was occurring. These included G85 in helix 1, G89 in loop 1, G91 in the helix 2, and R94, G95 in turn 1 of N-terminus. Residues D97 in face 1, Q106 and T107 in face 3, and Q111 in face 4 of coil 1; F134 in face 4 of coil 2, T139 in face 1, E145 in face 2, G150 in face 3, and F153 and S154 in face 4 of coil 3; N165 in face 2 of coil 4; and S182 in face 2 of coil 5 were also significantly influenced by temperature. L194 in the loop 2, L202, C203 in the helix 3, R218 in the helix 4, and the β-bridge A216 of C terminus experienced subtle changes with increasing temperature. Collectively, these residues likely indicated initiation sites for thermal unfolding in At2g44920.

Amide hydrogen exchange rates

Residue-resolved hydrogen exchange data were collected for most residues in AT2g44920 (Table S1) and fit to exponential decays to obtain exchange rates (Fig. S3). Slowly exchanging residues were quantified from hydrogen deuterium exchange experiments. Representative data used to calculate slow amide exchange rates are presented in Fig. S4. Fast amide proton exchange rates were quantified by CLEANEX-PM experiment (13). Example data from the CLEANEX-PM experiment and fits to obtain fast exchange rates are shown in Figs. S5 and S6, respectively. Amide exchange rates were plotted as a function of amino acid position in Fig. 5. Most fast exchanging amide hydrogens of AT2g44920 were located in the N-terminus, along with a few in the Rfr-fold core and C terminus. These residues were D97 ($i-1$, face 1), D102 ($i-1$, face 2), T107 ($i-1$, face 3), L118 (i, face 1), G125 ($i+2$, face 2), K127 ($i-1$, face3), S154 ($i+2$, face 4), L155 ($i+2$, face 4), D197 (C-terminal, α-helix), and C203 (C-terminal, α-helix). Most of these residues were located in position $i-1$ and $i+2$ of the pentapeptide repeat in coil 1 or coil 2. Based on DSSP motif classification and dihedral torsion angles of the amino acids, the $i-1$ residue in each pentapeptide repeat is defined as a β-bridge and the $i+2$ residue is defined as a bend. These fast-exchanging residues in the Rfr-fold shared the common feature that all of their side chains pointed away from the Rfr core, except for L118, which is stacked against coil 1 at the N-terminus. Most slowly exchanging residues were located in the Rfr-fold core, with some located in the C terminus. Interestingly, the exchange rates of amino acids determined from HDX experiments varied by several orders of magnitude even within the Rfr-fold core.

Activation energies for amide hydrogen exchange

HDX exchange rates were measured at three different temperatures, 298, 308, and 313 K to enable calculation of activation energies for amide hydrogen exchange by fitting to the Arrhenius equation (Fig. S7). Activation energies for amide hydrogen exchange were measured to provide insight into possible contributions from coil stacking interactions as a factor creating resistance to local unfolding and hydrogen bond

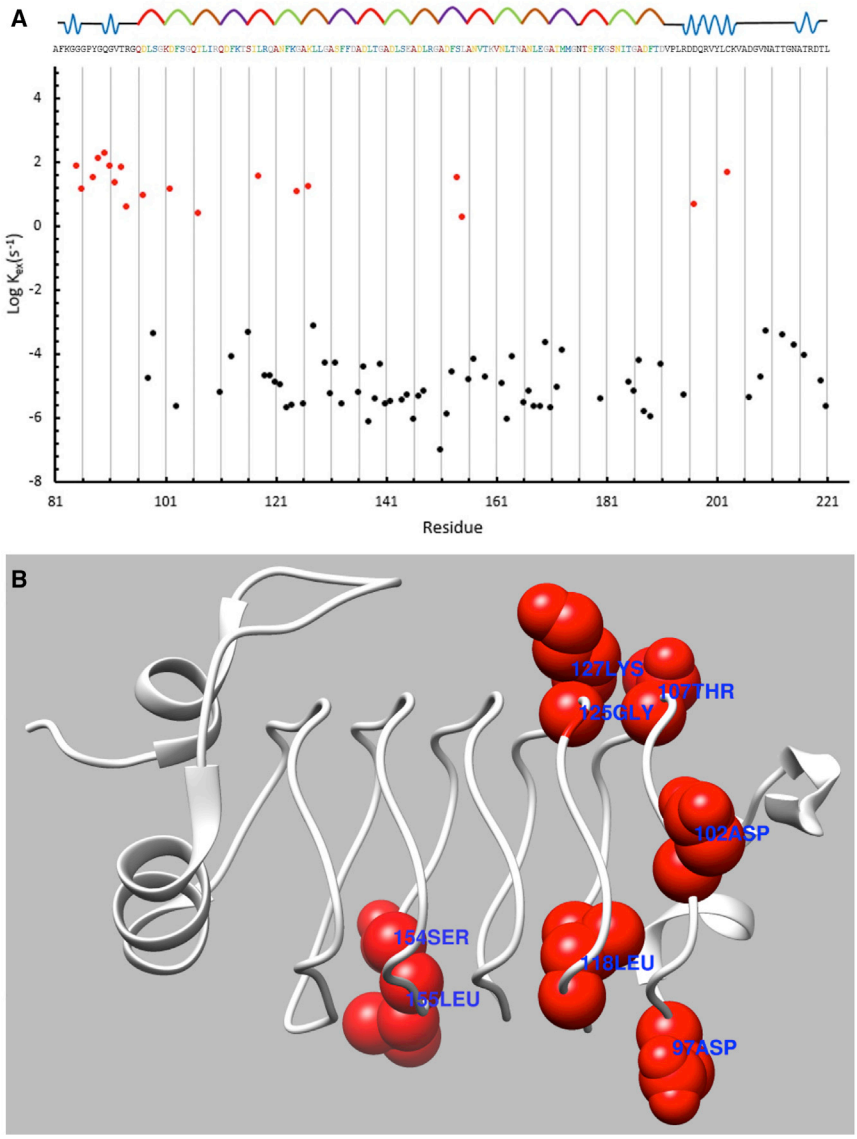

FIGURE 5 Amide hydrogen exchange rates plotted as a function of amino acid residue. (*A*) The logarithm of ^{1}H exchange rates are plotted versus residue number. Hydrogen exchange rates were measured by CLEANEX-PM (*red points* with Log K_{ex} values in the range 0–2 s^{-1}) or ^{1}H-^{15}N HSQC (*black*). (*B*) Shown here is a solid-sphere rendering of side chains of amino acids with fast-exchanging amide protons residing in Rfr coils. To see this figure in color, go online.

breaking required for exchange. Activation energies for individual amino acids were mapped onto the structure of At2g44920 in Fig. 6. As expected, amino acids with the highest activation energies for amide hydrogen exchange were found in the Rfr-fold core, consistent with a highly stable structure that is strongly resistant to amide hydrogen exchange (Fig. 7). Amino acids with the largest activation energies ($E_a > 200$ kJ/mol) were found in the center of coil 3 of the Rfr-fold: these residues included A136, L138, D142, S144, A146, D147, L148, A151, and F153. Additional residues with high activation energies ($E_a > 200$ kJ/mol) not in the central coil included Q111 ($i-2$, face 4) in coil 1; L163 (i, face 2) and A166 ($i-2$, face 3) in coil 4; and A187 ($i-2$, face 3) and F189 (i, face 3) in coil 5. Amino acids in the outer four coils on either of the Rfr-fold had low or intermediate activation energies ($E_a < 200$ kJ/mol). The observation that the activation energies for hydrogen bond exchange were highest in the middle of the Rfr core is consistent with the requirement that breaking of amide hydrogen bonds at the center of the coil requires concerted motion of multiple coils and this requires greater activation energy compared to breaking of amide hydrogen bonds in coils nearer the C- or N terminus, which only requires motion of a terminal coil and this results in smaller activation energies at either end of the At2g44920 β-helix. Some amino acids in the C-terminal loop or α-helices also had relatively small activation energies.

Backbone dynamics from amide ^{15}N relaxation measurements

Relaxation data at two different magnetic fields were obtained for 122 out of 138 residues assigned in At2g44920 (Table S3). Variations in the R_1 and R_2 values as a function

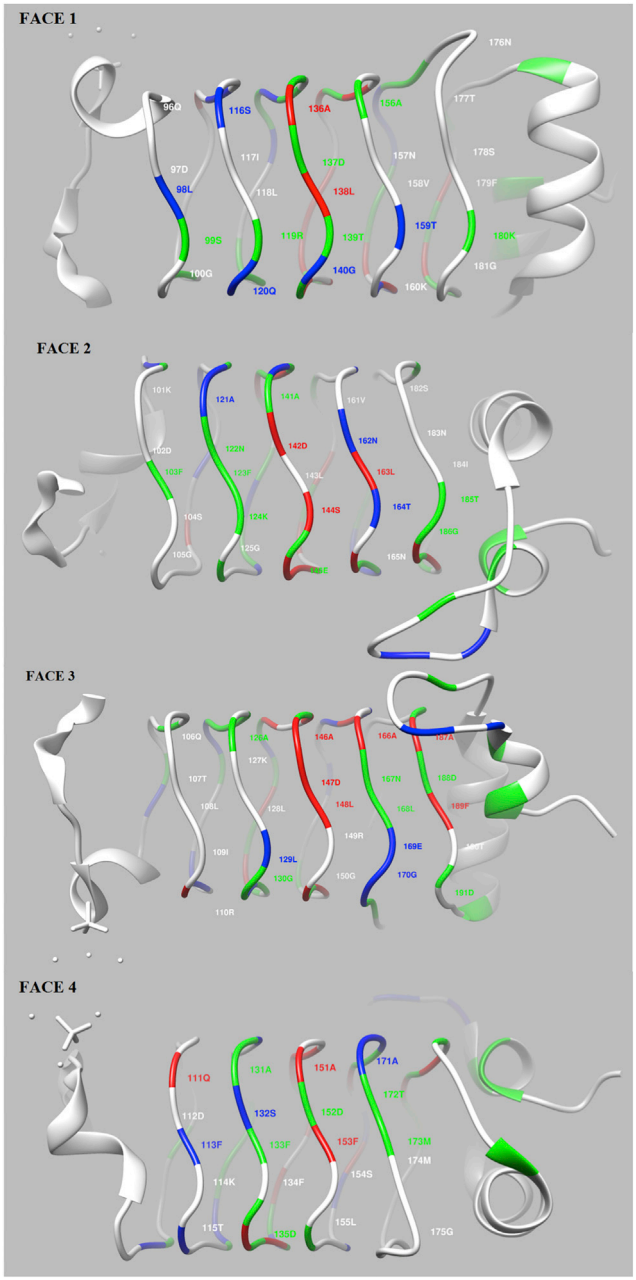

FIGURE 6 Shown here are the activation energies for amide hydrogen exchange mapped onto the crystal structure of At2g44920. The color scheme is based on the value of activation energy: white, undetermined; blue (*black*), <100 kJ/mol; green (*light gray*), 101–200 kJ/mol; red (*dark gray*), >200 kJ/mol. To see this figure in color, go online.

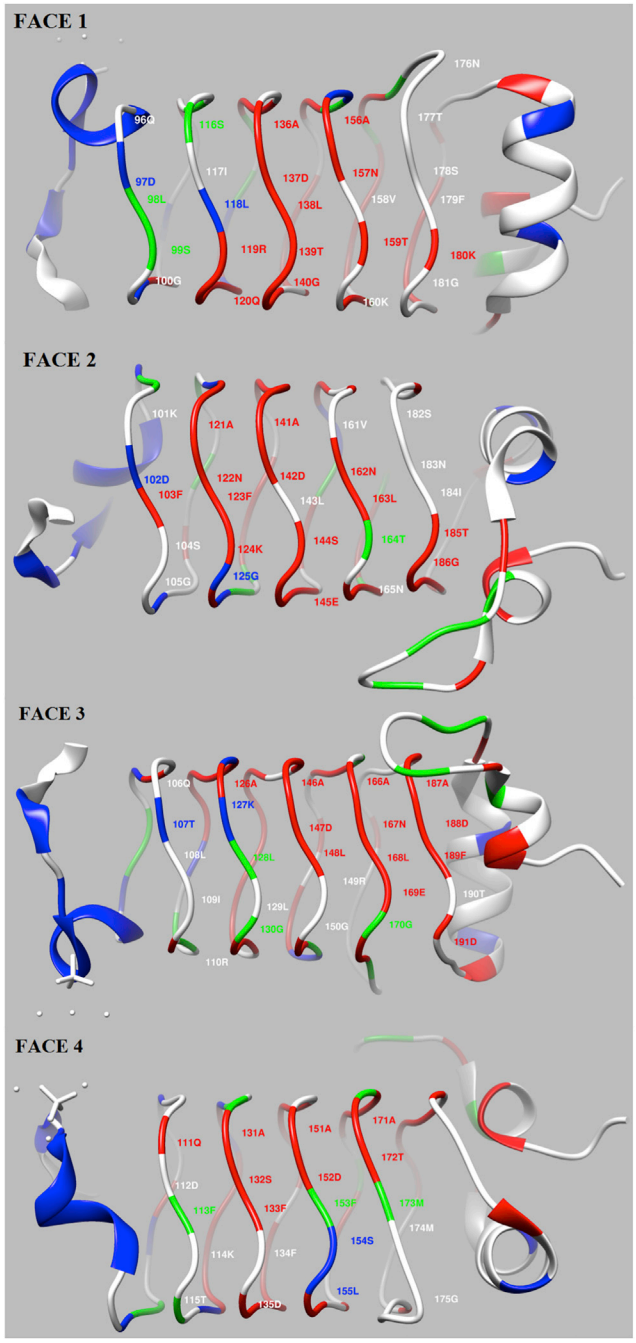

FIGURE 7 The logarithm of protection factors mapped onto the structure of At2g44920. The color-coding is as follows: white, undetermined; blue (*black*), 0–2; green (*light gray*), 4–6; red (*dark gray*), >6. To see this figure in color, go online.

of residue number at two different magnetic fields can be seen in Fig. 8. A clear pattern was apparent in the plotted R_1 values, where the $i-2$ and $i+1$ residues had the largest R_1 values, i.e., the shortest T_1 values, and the i and $i-1$ values had the smallest R_1 values, i.e., the longest T_1 values. To test if the data collected at 600 and 850 MHz were consistent, the spectral density at zero frequency was calculated using the reduced spectral density approach for the relaxation data at both fields. The ratio of $J(0)$ at two magnetic fields, plotted in Fig. S8, was centered around 1, indicating the relaxation data at the two magnetic fields were consistent with each other. The results of optimization of four diffusion tensors are summarized in Table S4, and the oblate spheroid model was selected based on the χ^2 values and AIC selection. Nine models were used to fit the

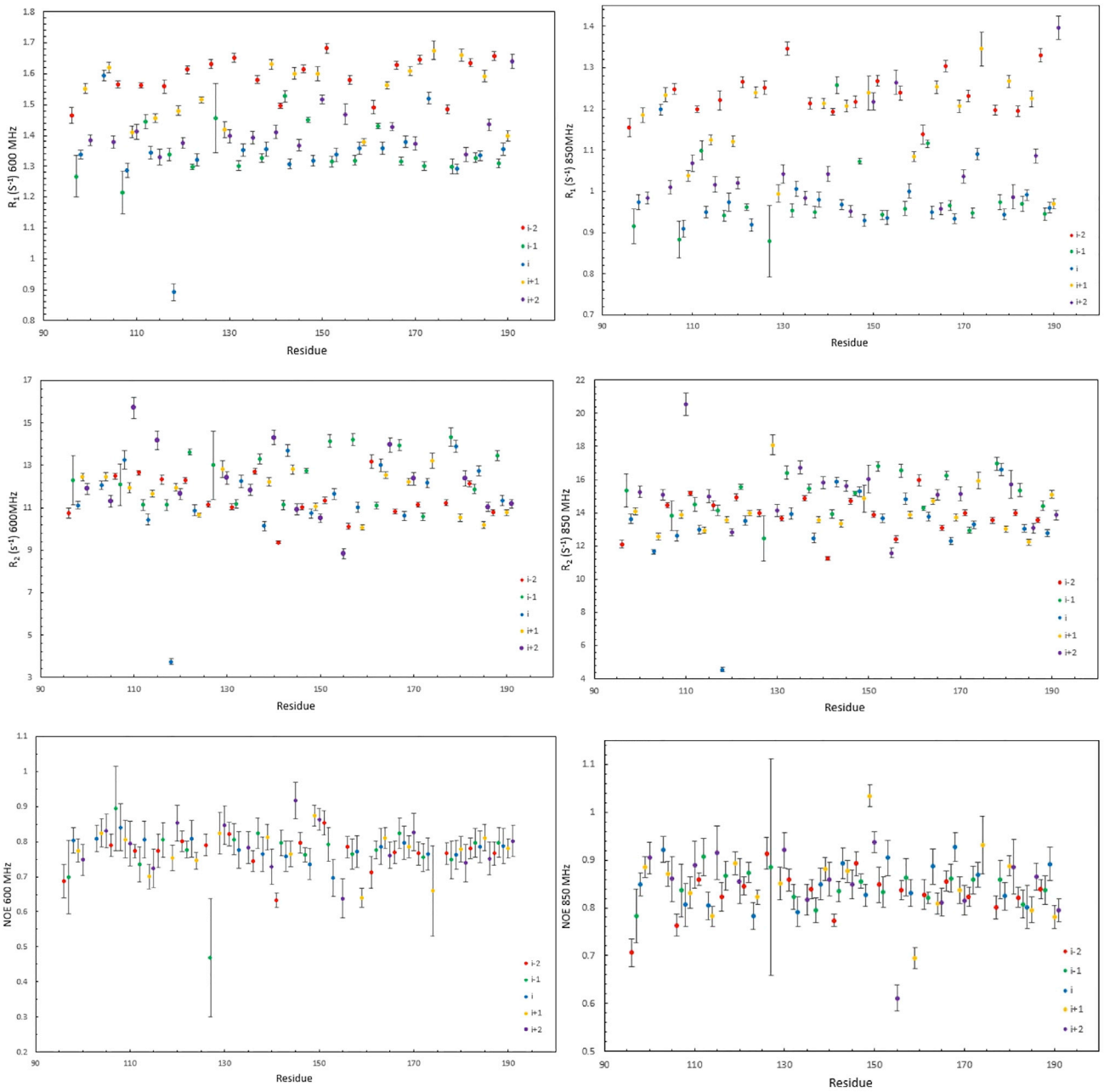

FIGURE 8 Plots of R_1, R_2, and ^{1}H-^{15}N NOE of At2g44920 as a function of residue number at two different magnetic fields of 600 and 850 MHz. Values are plotted for residues in the pentapeptide repeat sequence and colored/shaded according to the position within the pentapeptide repeat. To see this figure in color, go online.

relaxation parameters. Table S3 summarizes the model selection for each amino acid based on the F-tests. All generalized order parameters S^2 and the values of R_{ex} values measured at 600 and 850 MHz were plotted as a function of residue position in Fig. S9. The average value of the order parameters S^2 for At2g44920 was 0.79. The N-terminal region and a few residues in the Rfr-fold core and C-terminal were more disordered than the average on the picosecond timescale based on the order parameter analysis. These residues are Tyr-88, Gly-89, Arg-94, Leu-118, Ala-141, Cys-203, and Asp-207. Specifically, the average S^2 value for slow exchanging residues was 0.82, whereas the average S^2 value for fast exchanging residues was 0.58 (Fig. 9). The order parameters for the slowly exchanging residues were significantly larger than those for fast exchanging residues based on a Welch's t-test ($p = 0.025 < 0.05$), suggesting that residues experiencing slow hydrogen exchange tended to be rigid on the fast motion timescale. More careful examination of the order parameters revealed a pattern within the PRP (Fig. 10). Specifically, the $i-2$ (average

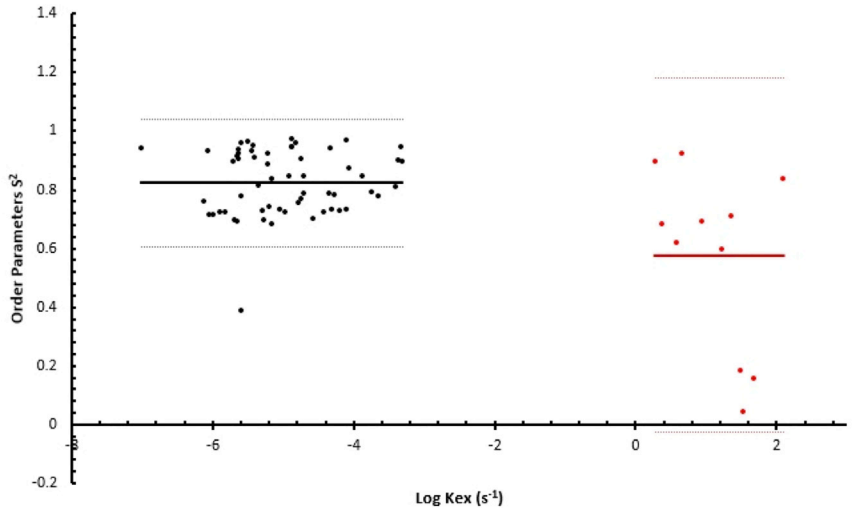

FIGURE 9 Order parameters plotted as a function of the logarithm of hydrogen exchange rate for each amino acid. Exchange rates were measured either by CLEANEX-PM experiments (*red points* with Log K_{ex} values in the range 0–2 s^{-1}) or ^{1}H-^{15}N HSQC experiments (*black*). Solid lines indicate mean values and dashed lines indicate ±95% confidence intervals. To see this figure in color, go online.

$S^2 = 0.89$) and $i+1$, (average $S^2 = 0.88$) positions in the pentapeptide repeat had relatively high-order parameter values, whereas the $i-1$ (average $S^2 = 0.75$) and i (average $S^2 = 0.71$) positions had relatively small order parameters, and the $i+2$ position had an intermediate value (average $S^2 = 0.80$). The results are summarized in Table 1. In attempting to understand these patterns in order parameters, we note that the amide group hydrogen atom in $i-2$ position forms an intracoil hydrogen bond with the amide carbonyl of i residue in the previous pentapeptide repeat (Fig. 2 *C*), and that this hydrogen bond represents a critical and universal structural feature of the Rfr fold, so it is not surprising this is a rigid structural element. Likewise, the $i+1$ amide vector is highly rigid because the carbonyl of the i residue forms an intracoil hydrogen bond with the $i-2$ amide hydrogen (Fig. 2 *C*), and this severely restricts this ϕ-angle with the $i+1$ amide group. The i and $i-1$ amides, which experience the largest fast timescale motion in the Rfr fold, form intercoil hydrogen bonds with the $i-1$ and $i-2$ carbonyls, respectively, of the following coil in the N- to C-terminal direction (Fig. 2 *D*). These hydrogen bonds define the β-ladder structure of the Rfr fold, which is the only other structural element of the Rfr fold besides the type II β-turns, and therefore it is not surprising that these amides are a stable and rigid structural element in At2g44920. However, the intercoil breathing apparently allows more fast timescale motion compared to the highly rigid intracoil type II β-turns. The $i+2$ amide experiences a magnitude of fast timescale motion intermediate between the highly rigid $i-2$ an $i+1$ residues and the relatively flexible i and $i-1$ residues. This can be rationalized because the $i+2$ amide forms an intercoil hydrogen bond with the $i+1$ residue carbonyl of the following coil, but its motion is restricted because it resides in the highly rigid type II β-turn.

Structural factors affecting amide hydrogen exchange

In a well-folded protein, exchangeable amide hydrogens involved in hydrogen bonds can only exchange with solvent

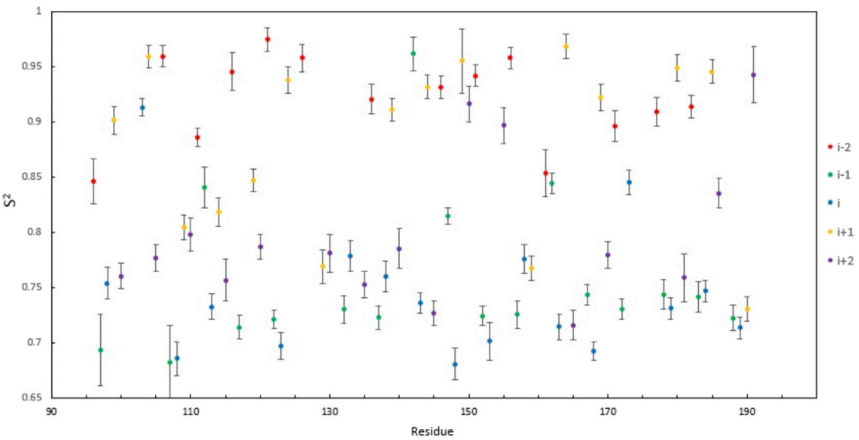

FIGURE 10 Order parameters plotted versus residue number in the Rfr-fold region of At2g44920. Points are colored/shaded (according to legend) according to sequence position in the pentapeptide repeat according to $i-2$ (*red*), $i-1$ (*green*), i (*blue*), $i+1$ (*yellow*), and $i+2$ (*purple*). To see this figure in color, go online.

TABLE 1 Mean Order Parameter Values for Amino Acid at each Position of the Pentapeptide Repeat

Position	Mean S^2	Standard Deviation
$i-2$	0.89	0.14
$i-1$	0.75	0.08
i	0.71	0.18
$i+1$	0.88	0.08
$i+2$	0.80	0.07

TABLE 2 Average Hydrogen Bond Energies and Solvent-accessible Surface Areas Grouped by Protection Factor Range

Log Protection Factor	Hydrogen Bond Energy (kcal/mol)	Surface-Accessible Area (Å^2)
Undetermined	−1.22	19.54
0–3	−1.20	14.21
4–6	−1.84	6.17
6–9	−1.89	9.11

when the hydrogen bond is transiently broken (24). Therefore, a successful amide hydrogen exchange event requires local or concerted protein motion to break the hydrogen-bond protection and allow the solvent to attack the amide hydrogen site. As the hydrogen exchange rates of exposed amides in unstructured polypeptides at different pH and temperature can be accurately predicted (44,45), protection factors can be used to quantify reduced rates of hydrogen exchange in structured proteins compared to in unfolded and unprotected polypeptides. The protection factors calculated for individual amino acids in At2g44920 were mapped onto the crystal structure in Fig. 7. A strong pattern was evident where the amino acids residing in the coils had the largest protection factors, except for coil 1, which lacks a stacking coil at its N-terminus. Finally, we examined if there was any pattern between protection factor and position within the pentapeptide repeat sequence by plotting the log of the protection factors as a function of residue in Fig. S10. This plot revealed no obvious pattern between protection factors and position within the PRP sequence.

One might expect that amide groups with smaller solvent-exposed surface areas would have larger protection factors because some theories suggest that HX rates reflect solvent accessibility (46,47). Based on visual inspection of the results in Fig. S11, a simple inverse relationship between protection factor and solvent-accessible surface area was not apparent. Rather, the solvent-accessible surface areas ranged from 0 to 45 Å^2 (Table S2) and were distributed across the entire range of protection factors for amino acid, which ranged from 0 to >8 (Table S1), indicating the solvent-accessible surface area was not a major factor to determine amide exchange rates. Analysis of the log of the protection factors groups into four crude bins of below detection, 0–3, 4–6, and 6–9, revealed that amide groups with protection factors below the detection limit had the highest average solvent-exposed surface areas of ∼19 Å^2, followed by amides in the smallest bin of 0–3 that had average solvent-exposed surface area of ∼14 Å^2 compared to those in 4–6 and 6–9 bins, which fell in the range of 6–9 Å^2 (Table 2).

In the context of the well-defined hydrogen-bonding network of the type II β-turns in At2g44920, nearly all amide hydrogens in the Rfr-core were strongly protected from exchange. However, no correlation between protection factors and hydrogen bond energies was obvious based on visual inspection (Fig. S12). However, again, grouping of the protection factors into three crude bins did reveal a weak trend correlating protection factor hydrogen bond energies (Table 2). Residues whose protection factors were smaller than the detection limit of the NMR techniques had average hydrogen bond energies of −1.22 kcal/mol (Table 2). Residues with protection factors from 0 to 3, which are not strongly protected from solvent exchange, had average hydrogen bond energies of −1.20 kcal/mol. Residues with protection factors ranging from 4 to 6 had average hydrogen bond energies of −1.84 kcal/mol. Amino acids with protection factor values ranging from 6 to 9, i.e., those most strongly protected from exchange, had average hydrogen bond energies of −1.89 kcal/mol. Despite the lack of any strict correlations among protection factor, hydrogen bond energy, and solvent-exposed surface area, on average, a clear trend emerged that the hydrogen bond energies steadily increased and the solvent-accessible surface areas gradually decreased as the protection factors increased.

DISCUSSION

At2g44920 is the first PRP protein, to our knowledge, whose subcellular location has been determined to be in the thylakoid lumen of *A. thaliana*. However, its precise biochemical function remains unknown. Given the unique β-helix structure of At2g44920 whose β-turns of the right-handed quadrilateral β-helix, or Rfr-fold, are exclusively type II β-turns, we decided to investigate whether it had any unusual biophysical properties such as exceptional stability, hydrogen bond strengths, or amide hydrogen exchange rates. Emberly et al. (48) pointed out that the parallel β-sheets in Rfr folds are very rigid and the architecture of the Rfr-fold may be especially sturdy. The CD melting results confirmed that At2g44920 was thermodynamically stable but not exceptional, falling at approximately the average melting temperature among values reported for >1100 proteins (Fig. S1 *D*). NMR-based measurements of backbone dynamics at different timescales confirm that the Rfr-fold is very rigid, especially within the Rfr fold core. Interestingly, we observed that the amide ^{15}N R_1 values adopted a pattern within the pentapeptide repeat sequence with $i-2$ and $i+1$ positions having the highest R_1 values and the i and $i-1$ positions having the smallest R_1 values. Residues in the $i-2$ and $i+1$ positions also had the largest order parameters, indicating the

smallest amplitude of fast motion within the Rfr core and the i and $i-1$ positions had the smallest order parameters corresponding to the largest amplitude fast motion within the Rfr core.

One of the most interesting aspects of our study was the observation that the amide hydrogen exchange rates spanned 10 orders of magnitude. Because the hydrogen-bonding pattern of the Rfr-fold in At2g44920 is well defined from its crystal structure (8), it is an excellent model to study factors affecting amide hydrogen exchange rates. In the temperature range used in this study, the exchanges rates were temperature dependent and there was no evidence of mixing of different exchange rates into a global rate, indicating they are still in the EX2 region, so it was reasonable to interpret the experimentally determined hydrogen exchange rates as being due to local or subglobal motion. In a hydrogen exchange event, a dynamic structural rearrangement is required to change an amino acid in a protein from an exchange-incompetent state into an exchange-competent state, which requires both disruption of H-bond protection and exposure of the amide protons to the solvent HX catalyst. Almost all amino acids in the N-terminus of At2g44920 exchanged relatively fast, which may be due to larger protein motion occurring as the protein transiently unfolds in the N-terminus. Compared to the N-terminus, amino acids located in the C terminus had relatively slow exchange rates, probably because of the structural stability imparted by the cysteine disulfide bridge linking the two α-helices, contributing to protection of these amino acids from exchange. The majority of amino acids that were strongly protected from hydrogen exchange were located within the Rfr fold core. Core residues tended to form stronger hydrogen bonds and had smaller solvent-accessible surface areas.

Despite decades of research, the interpretation of HX data for individual amide protons in proteins remains challenging as the factors that govern hydrogen exchange rates in protein are complicated. Current models for amide hydrogen exchange have been tested with data collected on Staphylococcal nuclease (49). It was found that solvent accessibility and solvent penetration models could not well explain the fast hydrogen exchange and slow hydrogen exchange. Protection factors were not well predicted from molecular dynamics simulations incorporating packing density and local interactions. In their accompanying article, Skinner et al. (50) emphasized the role of H-bonding protection and the protein motion that exposes the amide protons to D_2O solvent. Consistent with their findings, we found that H-bond energies and solvent-accessible surface areas were only weakly correlated with protection factors. As suggested by the work of Skinner et al. (49,50), the energy required to break an amide hydrogen bond enabling an exchange event cannot be inferred by the local hydrogen bond geometry alone, but the secondary effects must also be considered, e.g., how much energy must be require to displace the surrounding protein structure to enable the hydrogen bond to be disrupted. To probe this idea, we measured the activation energies for hydrogen bond exchange and found that hydrogen bonds for residues in the central coil tended to have the highest activation energies, consistent with the idea that the surrounding coils must be displaced, perhaps by concerted motion, for the hydrogen bond to be broken enabling solvent attack, and this requires more energy compared to a residue that is not in the central coil; however, the activation energies were not strictly correlated with the protection factors.

We also investigated how slow and fast timescale motions might influence hydrogen exchange rates. We probed the correlation between internal motions of N-H bond vectors obtained from ^{15}N spin relaxation with their hydrogen exchange behavior. The global rotational diffusion of macromolecule and the internal motions of the bond vectors were extracted from the model-free analysis developed by Lipari and Szabo (51,52). The order parameters analysis indicated that fast-exchanging residues tended to have relatively small order parameters, which is consistent with residues whose H-N vectors are undergoing large amplitude fast motion having more rapid amide hydrogen exchange.

In conclusion, At2g44920 represents an extremely well-defined model system for investigating amide exchange rates in proteins, and it exhibits a remarkable range of exchange lifetimes spanning 10 orders of magnitude. Our results illustrate that consideration of activation energies of amide hydrogen exchange adds important insight into understanding and predicting amide hydrogen protection factors in proteins. Further advancement and progress in establishing a complete understanding of the factors governing amide exchange rates in proteins will require continued research and investigation.

SUPPORTING MATERIAL

Twelve figures and four tables are available at http://www.biophysj.org/biophysj/supplemental/S0006-3495(17)30432-0.

AUTHOR CONTRIBUTIONS

S.X. performed research, conducted data analysis, and contributed to writing the manuscript. S.N. contributed to study design, sample preparation, and data analysis. M.A.K. was responsible for study design, data analysis, and writing the manuscript.

ACKNOWLEDGMENTS

We thank Alexander Yarawsky in Professor Andrew Herr's Lab at Cincinnati Children's Hospital Medical Center for help with collection and interpretation of the circular dichroism spectroscopy data.

REFERENCES

1. Bateman, A., A. G. Murzin, and S. A. Teichmann. 1998. Structure and distribution of pentapeptide repeats in bacteria. *Protein Sci.* 7:1477–1480.
2. Yoder, M. D., N. T. Keen, and F. Jurnak. 1993. New domain motif: the structure of pectate lyase C, a secreted plant virulence factor. *Science.* 260:1503–1507.
3. Jenkins, J., and R. Pickersgill. 2001. The architecture of parallel β-helices and related folds. *Prog. Biophys. Mol. Biol.* 77:111–175.
4. Richardson, J. S. 1981. The anatomy and taxonomy of protein structure. *Adv. Protein Chem.* 34:167–339.
5. Shepherd, A. J., D. Gorse, and J. M. Thornton. 1999. Prediction of the location and type of β-turns in proteins using neural networks. *Protein Sci.* 8:1045–1055.
6. Wilmot, C. M., and J. M. Thornton. 1988. Analysis and prediction of the different types of β-turn in proteins. *J. Mol. Biol.* 203:221–232.
7. Buchko, G. W., S. Ni, …, M. A. Kennedy. 2006. Characterization of two potentially universal turn motifs that shape the repeated five-residues fold–crystal structure of a lumenal pentapeptide repeat protein from Cyanothece 51142. *Protein Sci.* 15:2579–2595.
8. Ni, S., M. E. McGookey, …, M. A. Kennedy. 2011. The 1.7 Å resolution structure of At2g44920, a pentapeptide-repeat protein in the thylakoid lumen of *Arabidopsis thaliana*. *Acta Crystallogr. Sect. F Struct. Biol. Cryst. Commun.* 67:1480–1484.
9. Palmer, A. G., 3rd 1993. Dynamic properties of proteins from NMR spectroscopy. *Curr. Opin. Biotechnol.* 4:385–391.
10. Palmer, A. G., 3rd 1997. Probing molecular motion by NMR. *Curr. Opin. Struct. Biol.* 7:732–737.
11. Palmer, A. G., 3rd 2001. NMR probes of molecular dynamics: overview and comparison with other techniques. *Annu. Rev. Biophys. Biomol. Struct.* 30:129–155.
12. Kleckner, I. R., and M. P. Foster. 2011. An introduction to NMR-based approaches for measuring protein dynamics. *Biochim. Biophys. Acta.* 1814:942–968.
13. Hwang, T. L., P. C. van Zijl, and S. Mori. 1998. Accurate quantitation of water-amide proton exchange rates using the phase-modulated CLEAN chemical EXchange (CLEANEX-PM) approach with a Fast-HSQC (FHSQC) detection scheme. *J. Biomol. NMR.* 11:221–226.
14. Bédard, S., L. C. Mayne, …, S. W. Englander. 2008. The foldon substructure of staphylococcal nuclease. *J. Mol. Biol.* 376:1142–1154.
15. Kempf, J. G., and J. P. Loria. 2003. Protein dynamics from solution NMR: theory and applications. *Cell Biochem. Biophys.* 37:187–211.
16. Jarymowycz, V. A., and M. J. Stone. 2006. Fast time scale dynamics of protein backbones: NMR relaxation methods, applications, and functional consequences. *Chem. Rev.* 106:1624–1671.
17. Igumenova, T. I., K. K. Frederick, and A. J. Wand. 2006. Characterization of the fast dynamics of protein amino acid side chains using NMR relaxation in solution. *Chem. Rev.* 106:1672–1699.
18. Clore, G., A. Szabo, …, A. Gronenborn. 1990. Deviations from the simple two-parameter model-free approach to the interpretation of nitrogen-15 nuclear magnetic relaxation of proteins. *J. Am. Chem. Soc.* 112:4989–4991.
19. Daragan, V., and K. Mayo. 1997. Motional model analyses of protein and peptide dynamics using ^{13}C and ^{15}N NMR relaxation. *Prog. Nucl. Magn. Reson. Spectrosc.* 31:63–105.
20. Jin, D., M. Andrec, …, R. M. Levy. 1998. Propagation of experimental uncertainties using the Lipari-Szabo model-free analysis of protein dynamics. *J. Biomol. NMR.* 12:471–492.
21. Berger, A., and K. Linderstrøm-Lang. 1957. Deuterium exchange of poly-DL-alanine in aqueous solution. *Arch. Biochem. Biophys.* 69:106–118.
22. Hvidt, A. 1964. A discussion of the pH dependence of the hydrogen-deuterium exchange of proteins. *C. R. Trav. Lab. Carlsberg.* 34:299–317.
23. Woodward, C. K., and B. D. Hilton. 1979. Hydrogen exchange kinetics and internal motions in proteins and nucleic acids. *Annu. Rev. Biophys. Bioeng.* 8:99–127.
24. Hvidt, A., and S. O. Nielsen. 1966. Hydrogen exchange in proteins. *Adv. Protein Chem.* 21:287–386.
25. Ferraro, D. M., N. Lazo, and A. D. Robertson. 2004. EX1 hydrogen exchange and protein folding. *Biochemistry.* 43:587–594.
26. Bai, Y., J. S. Milne, …, S. W. Englander. 1994. Protein stability parameters measured by hydrogen exchange. *Proteins.* 20:4–14.
27. Hu, W., Z. Y. Kan, …, S. W. Englander. 2016. Cytochrome *c* folds through foldon-dependent native-like intermediates in an ordered pathway. *Proc. Natl. Acad. Sci. USA.* 113:3809–3814.
28. Itzhaki, L. S., J. L. Neira, and A. R. Fersht. 1997. Hydrogen exchange in chymotrypsin inhibitor 2 probed by denaturants and temperature. *J. Mol. Biol.* 270:89–98.
29. Chu, R., W. Pei, …, Y. Bai. 2002. Relationship between the native-state hydrogen exchange and folding pathways of a four-helix bundle protein. *Biochemistry.* 41:7998–8003.
30. Bai, Y., and S. W. Englander. 1996. Future directions in folding: the multi-state nature of protein structure. *Proteins.* 24:145–151.
31. Neira, J. L., L. S. Itzhaki, …, A. R. Fersht. 1997. Hydrogen exchange in chymotrypsin inhibitor 2 probed by mutagenesis. *J. Mol. Biol.* 270:99–110.
32. Delaglio, F., S. Grzesiek, …, A. Bax. 1995. NMRPipe: a multidimensional spectral processing system based on UNIX pipes. *J. Biomol. NMR.* 6:277–293.
33. Goddard, T. D., and D. G. Kneller. SPARKY 3. University of California, San Francisco, CA.
34. Bahrami, A., A. H. Assadi, …, H. R. Eghbalnia. 2009. Probabilistic interaction network of evidence algorithm and its application to complete labeling of peak lists from protein NMR spectroscopy. *PLoS Comput. Biol.* 5:e1000307.
35. Hwang, T., S. Mori, …, P. van Zijl. 1997. Application of phase-modulated CLEAN chemical EXchange spectroscopy (CLEANEX-PM) to detect water−protein proton exchange and intermolecular NOEs. *J. Am. Chem. Soc.* 119:6203–6204.
36. Bieri, M., E. J. d'Auvergne, and P. R. Gooley. 2011. relaxGUI: a new software for fast and simple NMR relaxation data analysis and calculation of ps-ns and μs motion of proteins. *J. Biomol. NMR.* 50:147–155.
37. d'Auvergne, E. J., and P. R. Gooley. 2008. Optimisation of NMR dynamic models I. Minimisation algorithms and their performance within the model-free and Brownian rotational diffusion spaces. *J. Biomol. NMR.* 40:107–119.
38. d'Auvergne, E. J., and P. R. Gooley. 2008. Optimisation of NMR dynamic models II. A new methodology for the dual optimisation of the model-free parameters and the Brownian rotational diffusion tensor. *J. Biomol. NMR.* 40:121–133.
39. Greenfield, N. J. 2006. Using circular dichroism spectra to estimate protein secondary structure. *Nat. Protoc.* 1:2876–2890.
40. Holzwarth, G., and P. Doty. 1965. The ultraviolet circular dichroism of polypeptides 1. *J. Am. Chem. Soc.* 87:218–228.
41. Greenfield, N., and G. D. Fasman. 1969. Computed circular dichroism spectra for the evaluation of protein conformation. *Biochemistry.* 8:4108–4116.
42. Perczel, A., K. Park, and G. D. Fasman. 1992. Deconvolution of the circular dichroism spectra of proteins: the circular dichroism spectra of the antiparallel β-sheet in proteins. *Proteins.* 13:57–69.
43. Bava, K. A., M. M. Gromiha, …, A. Sarai. 2004. ProTherm, version 4.0: thermodynamic database for proteins and mutants. *Nucleic Acids Res.* 32:D120–D121.
44. Bai, Y., J. S. Milne, …, S. W. Englander. 1993. Primary structure effects on peptide group hydrogen exchange. *Proteins.* 17:75–86.
45. Connelly, G. P., Y. Bai, …, S. W. Englander. 1993. Isotope effects in peptide group hydrogen exchange. *Proteins.* 17:87–92.

46. Woodward, C., I. Simon, and E. Tüchsen. 1982. Hydrogen exchange and the dynamic structure of proteins. *Mol. Cell. Biochem.* 48:135–160.

47. Truhlar, S. M., C. H. Croy, …, E. A. Komives. 2006. Solvent accessibility of protein surfaces by amide H/^{2}H exchange MALDI-TOF mass spectrometry. *J. Am. Soc. Mass Spectrom.* 17:1490–1497.

48. Emberly, E. G., R. Mukhopadhyay, …, N. S. Wingreen. 2004. Flexibility of β-sheets: principal component analysis of database protein structures. *Proteins.* 55:91–98.

49. Skinner, J. J., W. K. Lim, …, S. W. Englander. 2012. Protein hydrogen exchange: testing current models. *Protein Sci.* 21:987–995.

50. Skinner, J. J., W. K. Lim, …, S. W. Englander. 2012. Protein dynamics viewed by hydrogen exchange. *Protein Sci.* 21:996–1005.

51. Lipari, G., and A. Szabo. 1982. Model-free approach to the interpretation of nuclear magnetic resonance relaxation in macromolecules. 1. Theory and range of validity. *J. Am. Chem. Soc.* 104: 4546–4559.

52. Lipari, G., and A. Szabo. 1982. Model-free approach to the interpretation of nuclear magnetic resonance relaxation in macromolecules. 2. Analysis of experimental results. *J. Am. Chem. Soc.* 104: 4559–4570.